Cite This: ACS Appl. Polym. Mater. XXXX, XXX, XXX-XXX

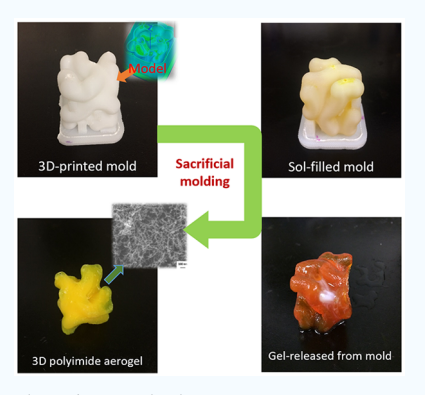
Development of Intricate Aerogel Articles Using Fused Filament Fabrication

Nicholas Teo,[†] Piljae Joo,[†] Eric J. Amis,*^{,‡} and Sadhan C. Jana*^{,†}

[†]Department of Polymer Engineering and [‡]Department of Polymer Science, The University of Akron, Akron, Ohio 44325, United States

Supporting Information

ABSTRACT: A fused filament fabrication process is used for conversion of polyimide aerogels into bicontinuous gyroid structures to obtain enhanced elasticity. A sacrificial hollow mold in an inverse gyroid shape is first fabricated from high impact polystyrene and is filled with the polyimide sol. After the sol—gel transition, the mold is dissolved in a solvent to yield the gel structure of a gyroid shape. The gel is supercritically dried to recover a free-standing aerogel structure with ultrahigh porosity (98.9%) and low bulk density (0.0146 g/cm³). The bicontinuous gyroid structure of the aerogel offers significant elasticity and high elongation at break compared to an otherwise brittle monolithic aerogel of polyimide. The ability to create intricate aerogel structures opens up a large potential in applications such as sensor housing and acoustic barriers of arbitrary shape and size and load-bearing porous thermally insulating structures that allow breathing.



KEYWORDS: aerogels, polyimide, fused filament fabrication, bicontinuous gyroid structure, low density, high porosity

INTRODUCTION

Downloaded by Sadhan Jana at 06:48:15:362 on June 09, 2019 from https://pubs.acs.org/doi/10.1021/acsapm.9b00301.

Aerogels are known for their high porosity (>90%), with pore sizes typically in the range of 10–200 nm and high surface areas, up to 1000 m²/g. The first aerogels reported in the literature were synthesized from silica by Kistler in the early 1930s.¹ The small pores of silica aerogels (50–200 nm) prohibit thermal transport through convection, resulting in low thermal conduction properties. Thus, silica aerogels were found suitable as thermal insulation materials for both the construction and aerospace industries. However, both their brittle nature and propensity for structural failure in the presence of moisture limited the implementation of pristine silica aerogels in commercial applications.

The aerogels synthesized from polymeric ingredients via the sol–gel transition² or thermoreversible gelation³ route present almost equivalent surface area and porosity values when compared to silica aerogels with large meso- and macropore fractions. In addition, polymeric aerogels have the added advantage of stronger mechanical properties. Polymeric aerogels synthesized from a variety of materials such as resorcinol–formaldehyde,⁴ syndiotactic polystyrene (sPS),⁵ poly(ether ether ketone) (PEEK),⁶ polyurea,⁷ polyurethane,⁸ and polyimide⁹ have subsequently been reported in the literature. A large majority of polymeric aerogels are synthesized from sol–gel processes, although aerogels of sPS and PEEK have been synthesized by using the thermoreversible gelation process. In terms of shapes, aerogel articles have been fabricated as monoliths,¹⁰ films,¹¹ membranes,¹² aerogel foams,^{13–15} and microparticles.^{16,17} It is important to note that literature on aerogel articles of complex geometrical shapes is

scarce due primarily to lack of appropriate fabrication techniques and high cost of tooling to retrofit conventional molding technologies.

As with silica aerogels, polymeric aerogels also find applications in thermal insulation, ¹⁸ with extended applications in aerospace industries. ¹⁹ The hierarchical meso- and macroporous structures of polymer aerogels were recently exploited in pursuing other applications, e.g., in high efficiency filtration of airborne nanoparticles. ^{20,21} Zhai and Jana ²⁰ and Kim, Chase, and Jana ²¹ reported successful filtration of airborne nanoparticles using aerogels, achieving 99.9% efficiency and air permeability values of the order of 10⁻¹⁰ m². We contend that rendering polymeric aerogels into articles of complex geometrical configurations may yield certain interesting properties and applications.

A number of complex three-dimensional (3D) structural forms can be produced by injection molding ²² and lithography²³ techniques. Some others, such as the bicontinuous gyroid structures, cannot be easily fabricated by the above tools due to difficulties associated with mold removal and 3D patterning. ²⁴ One may consider instead 3D printing technology based on the layer-by-layer assembly approach ^{25,26} which allows for greater degree of control in pore architecture, pore size distribution, and overall pore volume compared to traditional fabrication methods, such as those based on emulsion templating, porogen, and salt leaching techni-

 Received:
 March 30, 2019

 Accepted:
 May 28, 2019

 Published:
 May 28, 2019

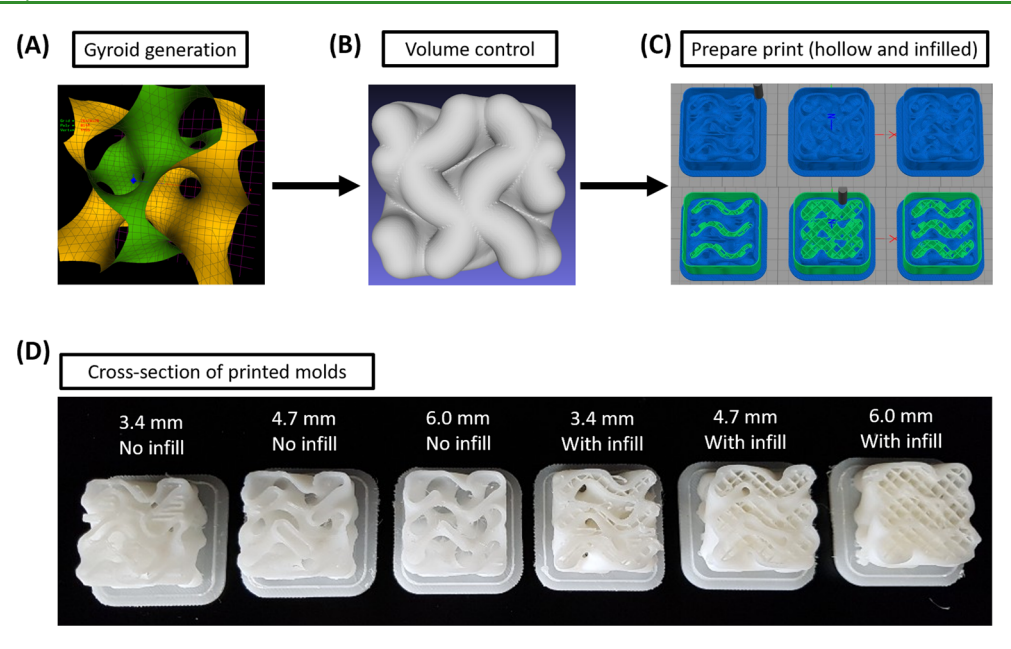


Figure 1. Illustration on preparation of gyroid molds. (A) Gyroid generation from eq 1 in K3DSurf. (B) volume generation by using Meshlab. (C) Cross section of CAD models. (D) Printed molds with different feature thicknesses.

ques.^{27,28} As is demonstrated in the present work, the 3D printing technology can be easily combined with systems undergoing sol—gel chemical reactions to obtain highly porous materials with hierarchical pores of a few tens of micrometers down to a few tens of nanometers.

The hierarchical porous structures can also be fabricated via the powder-based 3D printing method, ²⁹ e.g., by spraying a liquid onto a powder bed. The powder/liquid pairing undergoes either binding, chemical reactions, or crystallization to yield a hierarchical structure. This method, however, suffers from poor resolution and poor mechanical properties and is restricted by such parameters as powder flowability, stability, wettability, and reactivity to achieve stable free-standing structures. ³⁰

Another pathway to create hierarchical porous structures is 3D printing of gels, also known as direct ink writing (DIW), where a paste or a liquid is extruded and subsequently dried, gelled, or sintered.³¹ In this case, the macrostructure porosity is introduced and controlled via programmed movement of the delivery nozzle, while the inherent macro- or mesoporosity of the gel is ramified as macro- or mesopores in the final porous structures. Mesoporous bioactive glass scaffolds, successfully synthesized in this manner by Wu et al., 32 showed superior ion and drug release profiles. Minas et al.³³ used the DIW method in conjunction with emulsion and foam templating to obtain scaffolds with both micrometer and millimeter sized pores. Li et al.34-36 also successfully fabricated eco-friendly cellulosebased aerogels. However, this process is limited to only certain material systems, i.e., material systems with low viscosity to enable printing, yet possessing quick set times after printing to ensure dimensional integrity of the resultant structures.³⁷ Thus, it is apparent that processes such as DIW are limited to simple geometries and narrow working windows determined by the time scales of flow and that of cross-linking/setting reactions. The potential for structure collapse after extrusion is an additional limitation. 33,38 In view of the above limitations of DIW, the concept of 3D printing of hollow sacrificial molds was considered in this present work.

The 3D sacrificial hollow molds can be printed by using the stereolithography (SLA) technique from photopolymers soluble in water or alkaline solutions. 39-41 In this method, polymers or polymer precursors, such as silicone or urethane elastomers, are subsequently injected into the hollow mold and allowed to cure. Finally, the cured structure is recovered by dissolving the mold in NaOH solution. 42 Conventional organic solvents cannot dissolve the SLA printed parts due to their chemically cross-linked nature. Instead, aggressive solvents such as NaOH are needed to degrade the cross-linked network and release the SLA printed mold, although aggressive solvents such as NaOH solution can be detrimental to the gel structures. 43 The mold structure may also swell upon contact with the monomer, thus impacting the resolution and the mechanical properties of the sacrificial mold. These issues of SLA methods can be circumvented by considering 3D printing of sacrificial molds from a set of thermoplastic polymers. The use of thermoplastic polymers allows the usage of a larger set of solvents to dissolve the thermoplastic sacrificial molds without damaging the internal gel structures.

In this work, a facile method was developed for fabrication of hierarchical porous structures of gyroid shape with pores of a few tens of nanometers to a few micrometers. A sacrificial hollow mold of high impact polystyrene was printed directly by the fused filament fabrication method. We contend that this method may well serve as a platform technology for fabrication of gel and aerogel structures of complex shapes not previously achieved via customary tools such as injection molding or lithography. 44-46 The hollow bicontinuous gyroid mold of high impact polystyrene was used to obtain mesoporous polyimide gel of gyroid shape. The method adopted in this work is not restricted to only the gyroid geometry. It allows fabrication of aerogel metamaterials of arbitrary shape by independently controlling both the macrostructure geometry and the sol-gel chemistry. 47-49 The ability to create intricate aerogel structures, as exhibited in this work, opens up the potential for aerogels to expand applications in sensor housing and acoustic barriers of arbitrary shape and size and breathable

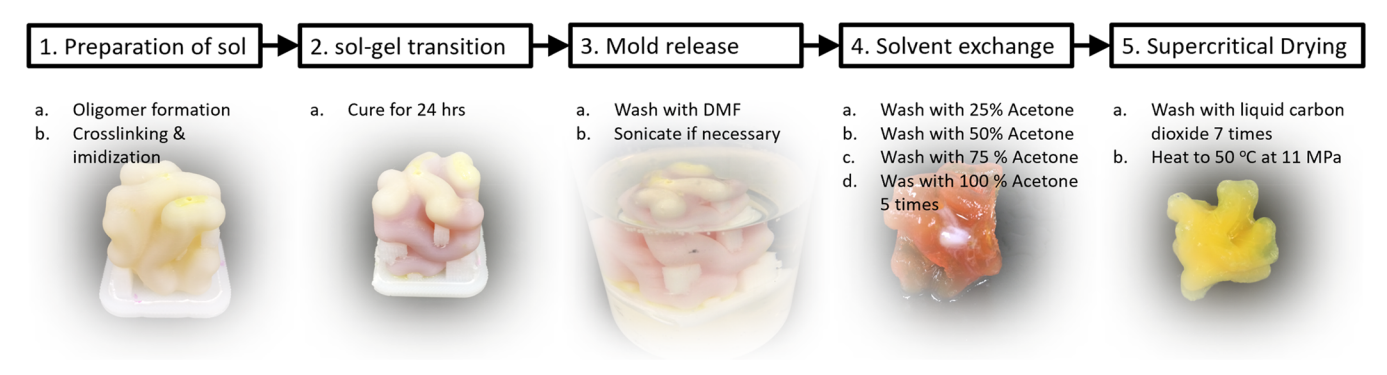


Figure 2. Procedure for polyimide aerogel synthesis.

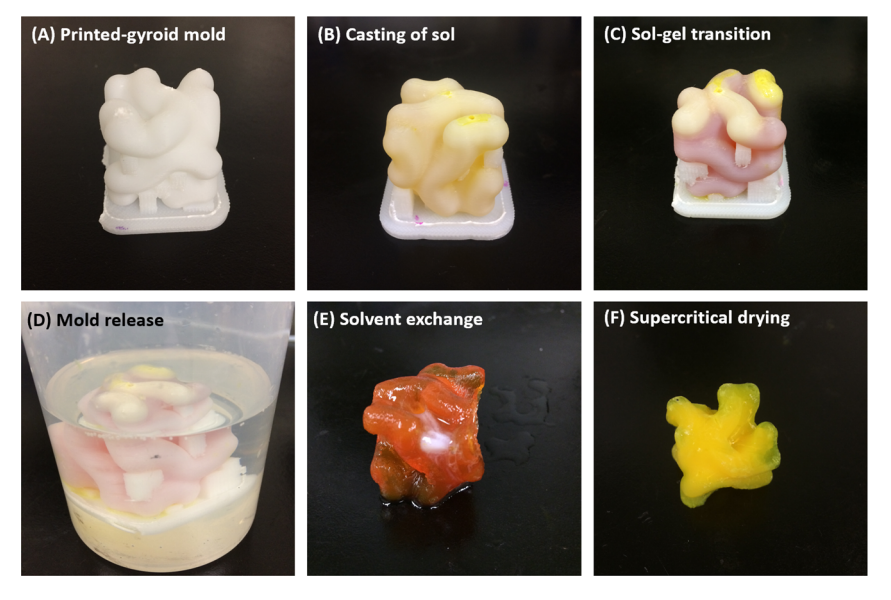


Figure 3. Synthesis of polyimide aerogel of gyroid shape through 3D printed hollow shells: (A) printed gyroid mold, (B) casted sol in mold, (C) sol—gel transition, (D) mold removal process, (E) solvent exchange, and (F) supercritical drying. The outer cuboidal dimensions (length \times width \times height) of the gyroid mold were 3 cm \times 3 cm \times 3 cm, respectively.

porous materials of arbitrary shape that simultaneously offer thermal insulation.

EXPERIMENTAL SECTION

Materials. Pyromellitic dianhydride (PMDA) was purchased from Alfa-Aesar (Haverhill, MA), and 2,2′-dimethylbenzidine (DMBZ) was purchased from Shanghai Worldyang Chemical Co. Ltd. (Shanghai, China). Tris(2-aminoethyl)amine (TREN) cross-linker was purchased from Sigma-Aldrich (Milwaukee, WI). Pyridine, acetic anhydride, and acetone were purchased from Fisher Scientific (Ontario, NY). N,N-Dimethylformamide (DMF) and dimethyl sulfoxide (DMSO) were purchased from VWR International (Radnor, PA). High-impact polystyrene (HIPS) filament was purchased from MatterHacker (Foothill Ranch, CA).

Fabrication of Sacrificial Mold. A bicontinuous gyroid structure was generated from an implicit equation (1)⁵⁰ in K3DSurf:

$$\sin x \cos y + \sin y \cos z + \sin z \cos x = 0 \tag{1}$$

The generated bicontinuous gyroid surfaces were subsequently imported into Meshlab and converted into volume models. The feature thickness of the volumes, defined as the width of the domain in the gyroid shape, was varied in this step in the range of 3.4–6.0 mm. Several representative images with feature thickness varying from 3.4 to 6.0 mm are presented in Figure 1. The Meshlab models were subsequently imported to Simplify3D, where the original filled model was converted into the hollow and infilled gyroid objects. This was achieved by controlling the density of infill of the model in

Simplify3D. For the hollow molds, a single extruder was used, while a double extruder set up was used for the molds with the infill. In the latter case, the secondary extruder was used to print the infill strands in an alternating manner ensuring that there was always a gap between the strands which could be subsequently filled by the precursor sol. In addition, to prevent leakage of the sol from the molds, the extrusion multiplier was set at 1.35 (distance between the strands), the outline printing speed was set at 1950 mm/min, and the infill printing speed was set at 3120 mm/min. The molds were printed with a Flashforge Creator Pro (Zhejiang, PRC) printer using HIPS filaments. HIPS filaments were specifically chosen as they were soluble in organic solvents such as DMF but resistant to dissolution in solvents used in polyimide synthesis, namely DMSO. A representative printing process with and without infill is shown in Figure 1.

Preparation of Polyimide Sol. The polyimide precursor solution (sol) was prepared at room temperature by mixing PMDA, DMBZ, and TREN in DMSO as the solvent, as per the process outlined by Teo and Jana. These dianhydride and diamine monomers were selected for two reasons. First, the presence of aromatic rings in these monomers along with the absence of flexible ether linkages is expected to produce greater mechanical strength in the resultant polymer backbone. Second, these monomers exhibit greater reactivity compared to other types of dianhydrides and diamines used typically in polyimide synthesis, thereby reducing the gel times. S2,53 Fast gel times were desired to minimize undesirable solvent evaporation prior to the sol—gel transition. Briefly, PMDA and DMBZ, dissolved individually in DMSO, were mixed with a magnetic stirrer at 1000 rpm for 2 min. This produced PMDA end-capped polyamic acid

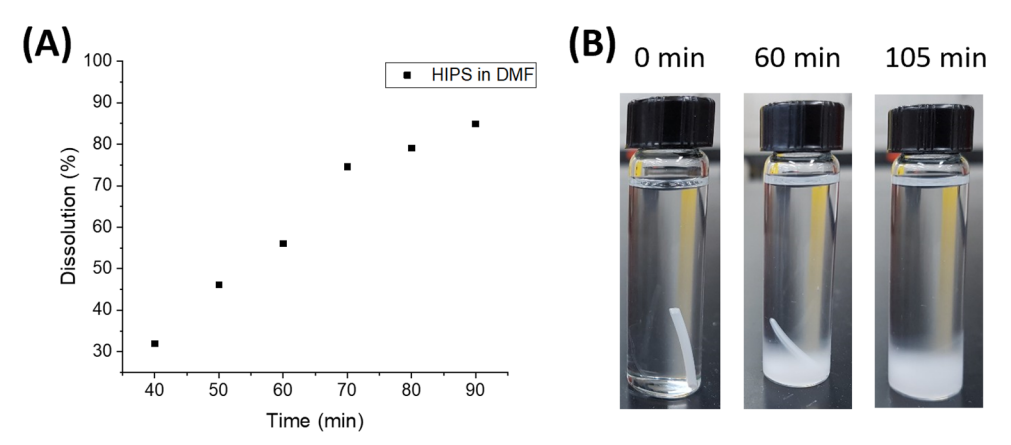


Figure 4. (A) Percent dissolution of HIPS with time. (B) State of HIPS filament in DMF after exposure for 0, 60, and 105 min.

oligomers. Subsequently, TREN, acetic anhydride, and pyridine were added, and the solution was magnetically stirred for an additional 1.5 min. The addition of these chemicals promoted both the cross-linking and chemical imidization reactions. A typical polyimide sol sample with 6.7 wt % polymer concentration was prepared using 0.42 g of PMDA, 0.42 g of DMBZ, 0.080 g of TREN, 1.33 g of acetic anhydride, 1.25 g of pyridine, and 10.0 mL of DMSO. A higher than stoichiometric amount of TREN cross-linker was used to obtain appropriate gelation times and stiffer gels.5

Synthesis of Polyimide Aerogels. Once the sol was prepared, it was transferred into a disposable syringe and injected into the 3Dprinted hollow mold. Typically, the sol takes about 27 min to transition into a gel. In this work, the sol was left to cure for an additional 24 h at room temperature to ensure that there was sufficient time for the majority of the cross-linking reactions to take place. After gelation, the mold was washed successively with DMF to dissolve and remove the HIPS exterior shell. For more intricate geometries, e.g., structures with infill or thin walls, sonication was required to effectively dissolve the HIPS portions from the crevices of the gel structures. In the next step, DMF solvent was removed from the inherently porous structure of the polyimide gel by solvent exchange with acetone. Note that DMF is not soluble in liquid carbon dioxide used in supercritical drying of the gel. The polyimide gels released from the mold were solvent-exchanged with acetone/DMF solvent mixtures. The solvent exchange was allowed to proceed for 12 h before replacing the solvent mixture with gradually higher acetone content. At the end, the samples were washed with 100% acetone for an additional five times to ensure that residual DMF was removed from the gel structure. The acetone-filled gels were subsequently solvent-exchanged with liquid carbon dioxide and dried under supercritical condition of carbon dioxide at 50 °C and 11 MPa pressure. The process described above is illustrated schematically in Figure 2. The images of actual sample in different stages of preparation are presented in Figure 3.

The total time of fabrication of an aerogel sample, starting from printing of the hollow molds to supercritical drying process, was ~1 week. This is in line with typical time taken in synthesis of aerogels with additional times contributed by 3D printing (~1 h) and mold release (~2 days). The long preparation time is attributed to the time needed for HIPS dissolution in the mold release step and diffusion of solvent in and out of the mesoporous gel structure during the solvent exchange step. It is noted that readily soluble mold materials or smaller size specimens would significantly reduce the total time. The preparation time can also be shortened using a sonication step.

Significant preliminary work was first conducted to determine the optimal pairings of synthesis solvent, mold release solvent, bridging solvent, and the materials for fabrication of the sacrificial molds. The selection of synthesis solvent was found to be crucial. For example, the synthesis solvent had to promote synthesis of the rigid gels without causing dissolution or swelling of the gyroid shell of HIPS. As presented earlier, DMF served as a solvent for removal of HIPS.

Figure 4 shows the dissolution rate of HIPS in DMF over time. Figure 4A shows that a large majority of HIPS (≈85%) was dissolved in 90 min. In view of this, molds were typically washed for 48 h to ensure that all HIPS were dissolved and removed from the gel.

The mold release solvent DMF was selected due to its miscibility with the synthesis solvent DMSO, which also reduced the interfacial stress in the gel structure and prevented structural collapse and shrinkage of the gel network during mold removal. The bridging solvent, acetone, was selected for its miscibility with DMF, DMSO, and liquid carbon dioxide.

This work primarily focused on process development to fabricate intricate aerogel articles by considering the gyroid structures of dimensions 3 cm \times 3 cm \times 3 cm as an example. The solvent and polymer pairings were just one of multiple potential combinations. We acknowledge that the process would involve large amounts of solvents for manufacturing large size articles. In light of this, we assessed the recyclability of the mold release solvent, namely DMF. Figure S1 in the Supporting Information shows that a majority of DMF could be recovered as the supernatant by centrifuging for 30 min the suspension obtained after dissolving the HIPS hollow shell mold. The reclaimed DMF was reused.

Characterization of Polyimide Aerogels. IR. Infrared spectra were collected on a Nicolet iS50 FTIR tridetector spectrophotometer (Thermo Scientific, Waltham, MA).

TGA. Thermogravimetric analysis (TGA) was conducted under N₂ with a Q50 thermogravimetric analyzer (TA Instruments, New Castle, DE) using a heating rate of 20 °C/min, up to 800 °C.

Porosity and Pore Volume. Porosity was calculated from the values of skeletal (ρ_s) and bulk density (ρ_b) as shown in eq 2. The values of skeletal density were obtained by using a helium pycnometer (AccuPyc II 1340, Micromeritics Instrument Corp., Norcross, GA). Bulk density was obtained from the mass and volume of the aerogels.

porosity =
$$\left(1 - \frac{\rho_b}{\rho_s}\right) \times 100\%$$
 (2)

Aerogel Morphology. The morphology of aerogels was studied by using a scanning electron microscope (SEM, JSM5310, JEOL, Peabody, MA) at an accelerating voltage of 5 kV and emission current of 20 mA. A representative piece of fractured aerogel specimen was mounted on an aluminum stub with carbon tape, followed by sputter coating with silver (ISI-5400 sputter coater, Polaron, London, UK).

Brunauer-Emmett-Teller (BET) Surface Area. The BET surface area of aerogel specimens was obtained from N2 adsorptiondesorption isotherms at 77 K by using a Micromeritics Tristar II 3020 analyzer (Micromeritics Instrument Corp., Norcross, GA).

Compressive Modulus. The compressive modulus of the aerogel samples was measured using an Instron 5567 tensometer (Norwood, MA). A 1 kN load cell was used with a compression rate of 1.3 mm/ min. The compressive modulus of the aerogels was obtained from the

slope of the stress-strain curve at a low strain, typically from 0.01 to 0.05 mm/mm.

RESULTS AND DISCUSSION

Polyimide aerogel structure synthesized by using the experimental method described above presented several distinct features. First, the complex aerogel geometry exhibited curved surfaces and recessed spaces. The method used in this work allowed easy release of the gel specimens from the hollow molds without damage. Second, the 3D-printed hollow molds allowed creation of hierarchical porous structures with high porosity. Figure 5 shows representative images of aerogels

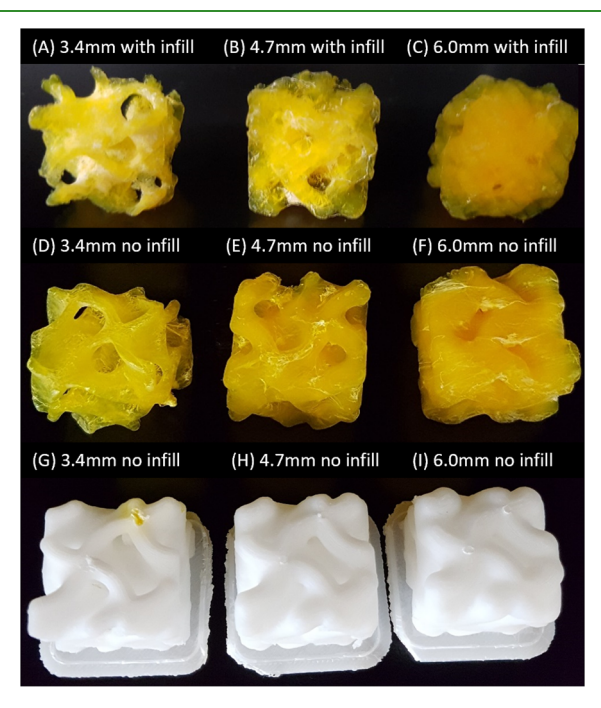


Figure 5. Polyimide aerogels (A-C) with infill and (D-F) without infill. (G-I) Hollow molds used in fabrication of the gyroid aerogels. The numbers in each of the figures refer to the feature thickness.

along with their corresponding 3D printed hollow molds. In this work, a low-cost, easily accessible fused filament printer was used to establish the proof-of-concept, with extruded strands of diameter 200 μ m. We acknowledge that the resolution of the printed hollow molds (and corresponding aerogels) can be improved using a fused filament printer with higher resolution. The surface roughness of the layer-by-layer filament structure in the hollow mold can also be alleviated by exposing the mold to acetone vapor as presented in Figure S2.

The aerogel specimens produced in this work exhibited both high porosity and low density, characteristic of aerogels, as shown in Table 1. For example, polyimide aerogel gyroids with feature thickness of 3.4 mm (Figure 5D) had a bulk density of 0.0308 g/cm³ and a porosity of 97.7%. The bulk density increased nearly linearly to 0.0534 g/cm³ as the feature thickness was increased to 6.0 mm (Figure 5F). The increase of bulk density also resulted in a reduction of porosity to 96.0% due to an increase of feature thickness. The gyroids with infill produced lower density and higher porosity than the normal gyroids. This was expected as the infill strands of HIPS added additional porosity to the structure after dissolution in DMF. This same trend in porosity and bulk density is reflected for the gyroids with infills, with the bulk density increasing from

Table 1. Bulk Density and Porosity as a Function of Feature Thicknessa

feature thickness (mm)	infill	bulk density, $ ho_{\rm b}~({ m g/cm^3})$	porosity (%)
control		0.0749	94.4
3.4	no	0.0308	97.7
4.7	no	0.0431	96.8
6.0	no	0.0534	96.0
3.4	yes	0.0146	98.9
4.7	yes	0.0225	98.3
6.0	yes	0.0322	97.6

^aThe top row (control) under "infill" column represents the hollow shells, the middle rows represent no infills, and the bottom rows represent specimens with infills.

0.0146 to 0.0322 g/cm³ and porosity decreasing from 98.9 to 97.6% for the same increase in feature thickness from 3.4 to 6.0 mm. The skeletal density was found to be consistent across all samples, registering a value of 1.34 ± 0.056 g/cm³. This was expected, as the skeletal density is determined by the chemical composition and the thermodynamics of gelation, independent of the macrostructure geometry. The images of corresponding hollow molds are presented in Figure 5G-I.

Figure 6A shows the IR spectrum of the polyimide aerogel. The presence of peaks at 730, 1380, 1716, and 1778 cm^{-1} indicates the presence of imide groups, while the lack of significant peaks at 1620 and 3000 cm⁻¹ indicates that the majority of polyamic acid was chemically converted into the imide functional groups. The TGA curve in Figure 6B shows that synthesized aerogels had high thermal stability, characteristic of polyimides. The polyimide exhibited a 5% weight loss at 443 °C, with the majority of degradation occurred at 550 °C. At 800 °C, the char yield was 55 wt %.

The aerogels also exhibited a high surface area of $579 \text{ m}^2/\text{g}$. The high BET surface area and high porosity of the structure are attributed to the fibrillar solid network structures of the polyimide strands shown in Figure 7A. These strands had a diameter of 14.3 \pm 2.7 nm as estimated from the SEM images. A type IV BET isotherm was observed as shown in Figure 7B, indicating significant mesopores in the polyimide aerogel

We next looked at the mechanical properties of these gyroid structures. Most of the aerogels exhibited similar stress-strain curves typical of porous materials, as described by Swyngedau.⁵⁴ To elucidate this behavior, we turn to the control aerogel sample, marked as the green curve in Figure 8A. This polyimide aerogel sample did not have complex geometry. The compression stress-strain curve of the aerogels can be divided into three broad regions. The first region, defined as the region from 0 to 0.1 mm/mm strain, involves the deformation of the aerogel structure, with the applied load borne by the skeletal structure of the polyimide strands. The second region is described by a plateau, characterized by the region from 0.1 to 0.6 mm/mm strain, whereby the skeletal structure was collapsed, and the pores of the aerogel structure underwent compression. Once all the pores were compacted, the stress-strain curve entered the third region. In the region of strain >0.6 mm/mm, the stress increased drastically as the applied load was carried by the compressed bulk polymer.

Comparing the stress-strain curves of the control sample with that of the gyroid-shaped samples, we note some differences in the stress-strain curves as shown in Figure 8. First, the gyroid structures with feature thicknesses of 4.7 and

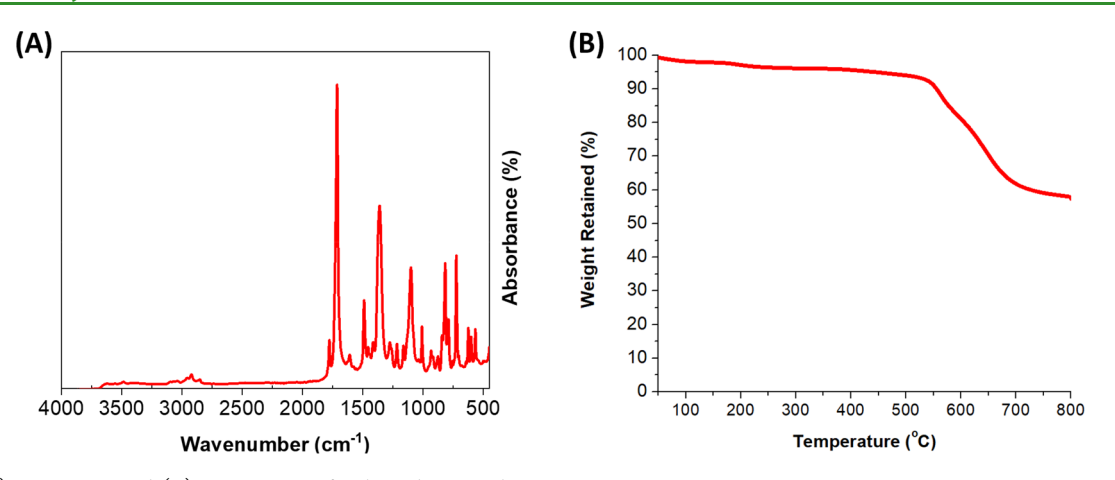


Figure 6. (A) IR spectra and (B) TGA curve of polyimide aerogel.

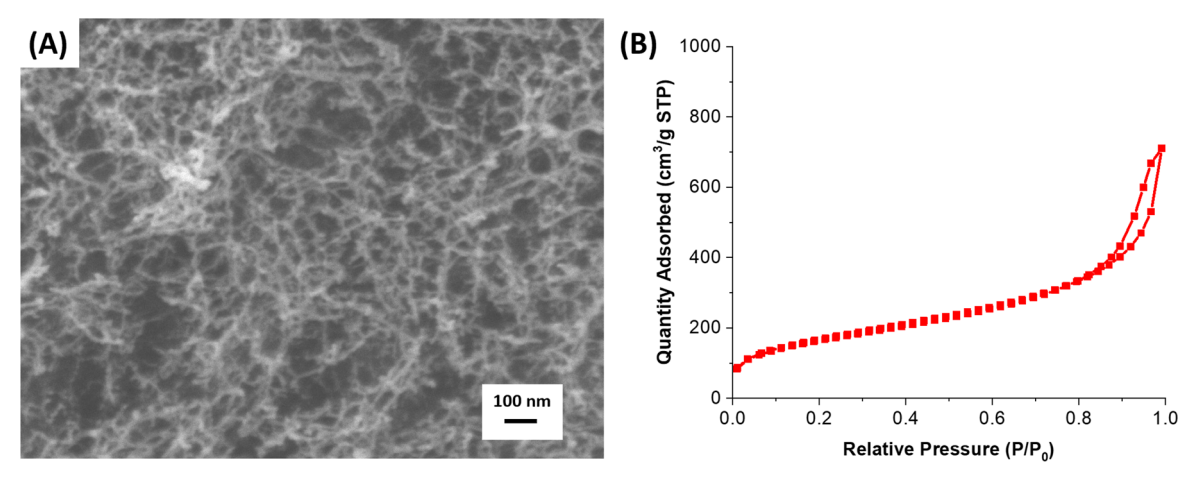


Figure 7. (A) SEM image of polyimide aerogel structure. (B) BET isotherm of polyimide aerogel.

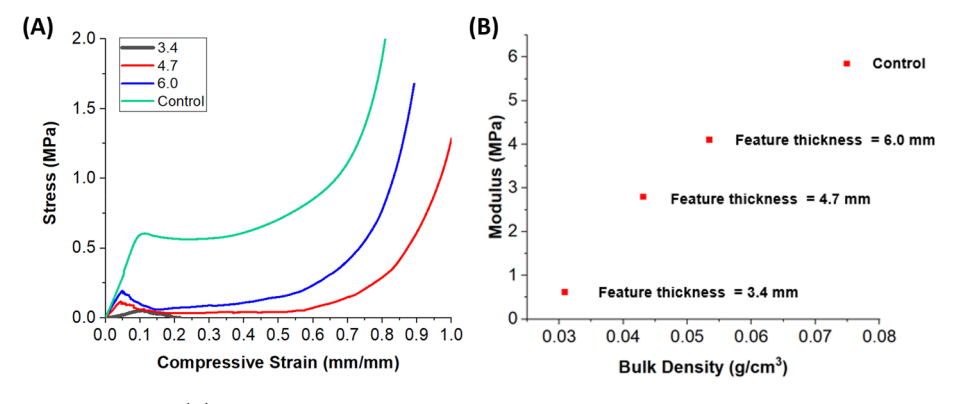


Figure 8. (A) Stress-strain curves and (B) compressive modulus vs bulk density of polyimide aerogels as a function of feature thickness.

6.0 mm exhibit the same stress—strain behavior as the control aerogel sample, with the three broad regions of deformation as described above. However, the gyroid structure with the feature thickness of 3.4 mm exhibited a brittle fracture at 0.2 mm/mm strain. This can be attributed to low bulk density of 0.0308 cm³/g and porosity of 97.7% of the structure. For this reason, the compression tests were not conducted on the samples with the infill, as their bulk density values were similar to or lower than that of this sample. Next, the stress—strain curves of specimens with 4.7 and 6.0 mm feature thicknesses showed initial brittle fracture of the structure after the first region. This is characterized by a drop in the stress value at the 0.06 mm/mm strain mark, before entering the second region

and subsequently plateauing out. This phenomenon was also observed visually, with crack formation and propagation in certain areas of the structure during the compression tests. This partial brittle fracture can be attributed to the geometry introduced through the gyroid structure, specifically to the collapse of the macro-interstitial spaces between the curved volumes of the gyroid. The second and third region of these structures are similar to those exhibited by the control samples.

We next investigated the effect of feature thickness on mechanical properties. The compressive modulus of the aerogel samples was measured at low strain, in the first region of the stress—strain curve. Figure 8B shows that the modulus varies linearly with bulk density. For example, the control

sample exhibited a compressive modulus of 5.85 MPa with a corresponding bulk density of 0.0749 g/cm³, while the gyroid structure with a feature thickness of 3.4 mm had a compressive modulus of 0.626 MPa with a corresponding bulk density of 0.0308 g/cm³. The compressive modulus of specimens with gyroid structures with increasing feature thickness shows a linear relationship between the above two values. This result is interesting in itself. For porous materials, the compressive modulus typically scales exponentially with the bulk density according to the Gibson and Ashby model.⁵⁵ In particular, porous materials follow a power-law relationship between bulk density, ρ_b , and compressive modulus (E) as $E \sim \rho_b^{\ \alpha}$, with foams exhibiting a value of α of 2, while for aerogels, a higher exponent α of 3.6 is reported. In our research, the almost linear dependence of modulus with bulk density translates into an exponent value α of close to 1, significantly lower than the reported values of α between 2 and 3.6. This result suggests that the gyroid geometry does impart some advantage for load bearing applications.⁵⁷ An analysis of the origin of lower value of α in this work is beyond the scope of the present report and will be covered in a future study.

CONCLUSION

The work demonstrates that additive manufacturing tools can be implemented in generation of aerogel structures with complicated shapes, such as the bicontinuous gyroid aerogel structures with curved surfaces and recessed spaces. The compatibility of sacrificial molding process enables quick fabrication of these structures through sol—gel chemistry that allows for extraction of the gel without damage to the structure. The 3D-printed aerogel structures show similar porosity and bulk density as the monoliths, but the compressive modulus varies proportionally with the bulk density in contrast to bulk density exponent of 2.0 for foams and 3.6 for aerogel monoliths.

ASSOCIATED CONTENT

S Supporting Information

The Supporting Information is available free of charge on the ACS Publications website at DOI: 10.1021/acsapm.9b00301.

Images of recyclability test of HIPS polymer and DMF solvent and SEM images of printed molds (PDF)

AUTHOR INFORMATION

Corresponding Authors

*E-mail janas@uakron.edu (S.C.J.).

*E-mail amis@uakron.edu (E.J.A.).

ORCID ®

Sadhan C. Jana: 0000-0001-8962-380X

Author Contributions

N.T. and P.J. contributed equally.

Notes

The authors declare no competing financial interest.

ACKNOWLEDGMENTS

This work was partially funded by National Science Foundation under Grant CMMI 1826030.

REFERENCES

(1) Kistler, S. S. Coherent Expanded Aerogels and Jellies. *Nature* 1931, 127 (3211), 741.

- (2) Leventis, N.; Chidambareswarapattar, C.; Bang, A.; Sotiriou-Leventis, C. Cocoon-in-Web-like Superhydrophobic Aerogels from Hydrophilic Polyurea and Use in Environmental Remediation. *ACS Appl. Mater. Interfaces* **2014**, *6* (9), 6872–6882.
- (3) Daniel, C.; Menelle, A.; Brulet, A.; Guenet, J. M. Thermoreversible Gelation of Syndiotactic Polystyrene in Toluene and Chloroform. *Polymer* 1997, 38 (16), 4193–4199.
- (4) Pekala, R. W. Organic Aerogels from the Polycondensation of Resorcinol with Formaldehyde. J. Mater. Sci. 1989, 24 (9), 3221–3227
- (5) Kim, S. J.; Chase, G.; Jana, S. C. The Role of Mesopores in Achieving High Efficiency Airborne Nanoparticle Filtration Using Aerogel Monoliths. Sep. Purif. Technol. 2016, 166, 48–54.
- (6) Talley, S. J.; Yuan, X.; Moore, R. B. Thermoreversible Gelation of Poly(Ether Ether Ketone). ACS Macro Lett. 2017, 6 (3), 262–266.
- (7) Shinko, A.; Jana, S. C.; Meador, M. A. B. Crosslinked Polyurea Aerogels with Controlled Porosity. *RSC Adv.* **2015**, *5* (127), 105329–105338.
- (8) Chidambareswarapattar, C.; McCarver, P. M.; Luo, H.; Lu, H.; Sotiriou-Leventis, C.; Leventis, N. Fractal Multiscale Nanoporous Polyurethanes: Flexible to Extremely Rigid Aerogels from Multifunctional Small Molecules. *Chem. Mater.* **2013**, *25* (15), 3205–3224.
- (9) Teo, N.; Jana, S. C. Solvent Effects on Tuning Pore Structures in Polyimide Aerogels. *Langmuir* **2018**, *34* (29), 8581–8590.
- (10) Kim, S. J.; Raut, P.; Jana, S. C.; Chase, G. Electrostatically Active Polymer Hybrid Aerogels for Airborne Nanoparticle Filtration. *ACS Appl. Mater. Interfaces* **2017**, *9* (7), 6401–6410.
- (11) Meador, M. A. B.; Malow, E. J.; Silva, R.; Wright, S.; Quade, D.; Vivod, S. L.; Guo, H.; Guo, J.; Cakmak, M. Mechanically Strong, Flexible Polyimide Aerogels Cross-Linked with Aromatic Triamine. ACS Appl. Mater. Interfaces 2012, 4 (2), 536–544.
- (12) Raut, P.; Liang, W.; Chen, Y. M.; Zhu, Y.; Jana, S. C. Syndiotactic Polystyrene-Based Ionogel Membranes for High Temperature Electrochemical Applications. *ACS Appl. Mater. Interfaces* **2017**, 9 (36), 30933–30942.
- (13) Gu, S.; Jana, S. C. Open Cell Aerogel Foams with Hierarchical Pore Structures. *Polymer* **2017**, *125*, 1–9.
- (14) Teo, N.; Jana, S. C. Open Cell Aerogel Foams via Emulsion Templating. *Langmuir* **2017**, 33 (44), 12729–12738.
- (15) Teo, N.; Gu, Z.; Jana, S. C. Polyimide-Based Aerogel Foams, via Emulsion-Templating. *Polymer* **2018**, *157*, 95–102.
- (16) Gu, S.; Zhai, C.; Jana, S. C. Aerogel Microparticles from Oil-in-Oil Emulsion Systems. *Langmuir* **2016**, *32* (22), 5637–5645.
- (17) Teo, N.; Jana, S. C. Surfactant-Free Process for the Fabrication of Polyimide Aerogel Microparticles. *Langmuir* **2019**, *35*, 2303–2312.
- (18) Feng, J.; Wang, X.; Jiang, Y.; Du, D.; Feng, J. Study on Thermal Conductivities of Aromatic Polyimide Aerogels. *ACS Appl. Mater. Interfaces* **2016**, *8* (20), 12992–12996.
- (19) Meador, M. A. B.; Wright, S.; Sandberg, A.; Nguyen, B. N.; Van Keuls, F. W.; Mueller, C. H.; Rodríguez-Solís, R.; Miranda, F. A. Low Dielectric Polyimide Aerogels as Substrates for Lightweight Patch Antennas. *ACS Appl. Mater. Interfaces* **2012**, *4* (11), 6346–6353.
- (20) Zhai, C.; Jana, S. C. Tuning Porous Networks in Polyimide Aerogels for Airborne Nanoparticle Filtration. ACS Appl. Mater. Interfaces 2017, 9 (35), 30074–30082.
- (21) Kim, S. J.; Chase, G.; Jana, S. C. Polymer Aerogels for Efficient Removal of Airborne Nanoparticles. *Sep. Purif. Technol.* **2015**, *156*, 803–808
- (22) Heckele, M.; Schomburg, W. K. Review on Micro Molding of Thermoplastic Polymers. J. Micromech. Microeng. 2004, 14 (3), R1.
- (23) Liu, C. Recent Developments in Polymer MEMS. Adv. Mater. **2007**, 19 (22), 3783–3790.
- (24) Harriott, L. R. Limits of Lithography. *Proc. IEEE* **2001**, 89 (3), 366–374.
- (25) Huang, S. H.; Liu, P.; Mokasdar, A.; Hou, L. Additive Manufacturing and Its Societal Impact: A Literature Review. *Int. J. Adv. Manuf. Technol.* **2013**, *67* (5–8), 1191–1203.

- (26) Wang, X.; Jiang, M.; Zhou, Z.; Gou, J.; Hui, D. 3D Printing of Polymer Matrix Composites: A Review and Prospective. *Composites, Part B* **2017**, *110*, 442–458.
- (27) Hollister, S. J. Porous Scaffold Design for Tissue Engineering. *Nat. Mater.* **2005**, 4 (7), 518–524.
- (28) Yoo, D. New Paradigms in Hierarchical Porous Scaffold Design for Tissue Engineering. *Mater. Sci. Eng., C* **2013**, 33 (3), 1759–1772.
- (29) Butscher, A.; Bohner, M.; Hofmann, S.; Gauckler, L.; Müller, R. Structural and Material Approaches to Bone Tissue Engineering in Powder-Based Three-Dimensional Printing. *Acta Biomater.* **2011**, 7 (3), 907–920.
- (30) Cox, S. C.; Thornby, J. A.; Gibbons, G. J.; Williams, M. A.; Mallick, K. K. 3D Printing of Porous Hydroxyapatite Scaffolds Intended for Use in Bone Tissue Engineering Applications. *Mater. Sci. Eng., C* 2015, 47, 237–247.
- (31) Truby, R. L.; Lewis, J. A. Printing Soft Matter in Three Dimensions. *Nature* **2016**, *540* (7633), 371–378.
- (32) Wu, C.; Luo, Y.; Cuniberti, G.; Xiao, Y.; Gelinsky, M. Three-Dimensional Printing of Hierarchical and Tough Mesoporous Bioactive Glass Scaffolds with a Controllable Pore Architecture, Excellent Mechanical Strength and Mineralization Ability. *Acta Biomater.* **2011**, *7* (6), 2644–2650.
- (33) Minas, C.; Carnelli, D.; Tervoort, E.; Studart, A. R. 3D Printing of Emulsions and Foams into Hierarchical Porous Ceramics. *Adv. Mater.* **2016**, 28 (45), 9993–9999.
- (34) Li, V. C. F.; Dunn, C. K.; Zhang, Z.; Deng, Y.; Qi, H. J. Direct Ink Write (DIW) 3D Printed Cellulose Nanocrystal Aerogel Structures. Sci. Rep. 2017, 7, 8018.
- (35) Li, V. C. F.; Mulyadi, A.; Dunn, C. K.; Deng, Y.; Qi, H. J. Direct Ink Write 3D Printed Cellulose Nanofiber Aerogel Structures with Highly Deformable, Shape Recoverable, and Functionalizable Properties. ACS Sustainable Chem. Eng. 2018, 6 (2), 2011–2022.
- (36) Li, V. C. F.; Kuang, X.; Hamel, C. M.; Roach, D.; Deng, Y.; Qi, H. J. Cellulose Nanocrystals Support Material for 3D Printing Complexly Shaped Structures via Multi-Materials-Multi-Methods Printing. *Addit. Manuf.* **2019**, 28, 14–22.
- (37) Smay, B. J. E.; Gratson, G. M.; Shepherd, R. F.; Cesarano, J.; Lewis, J. A. Directed Colloid Assembly of 3D Periodic Structures. *Adv. Mater.* **2002**, *14* (18), 1279–1283.
- (38) Hong, S.; Sycks, D.; Chan, H. F. A.; Lin, S.; Lopez, G. P.; Guilak, F.; Leong, K. W.; Zhao, X. 3D Printing of Highly Stretchable and Tough Hydrogels into Complex, Cellularized Structures. *Adv. Mater.* **2015**, *27* (27), 4034.
- (39) Liska, R.; Schwager, F.; Maier, C.; Cano-Vives, R.; Stampfl, J. Water-Soluble Photopolymers for Rapid Prototyping of Cellular Materials. *J. Appl. Polym. Sci.* **2005**, 97 (6), 2286–2298.
- (40) Park, J. H.; Jung, J. W.; Kang, H.-W.; Cho, D.-W. Indirect Three-Dimensional Printing of Synthetic Polymer Scaffold Based on Thermal Molding Process. *Biofabrication* **2014**, *6* (2), 025003.
- (41) Yoon, Y. K.; Park, J. H.; Allen, M. G. Multidirectional UV Lithography for Complex 3-D MEMS Structures. *J. Microelectromech. Syst.* 2006, 15 (5), 1121–1130.
- (42) Jiang, Y.; Wang, Q. Highly-Stretchable 3D-Architected Mechanical Metamaterials. Sci. Rep. 2016, 6, 34147.
- (43) Göpferich, A. Mechanisms of Polymer Degradation and Erosion. *Biomaterials* **1996**, *17* (2), 103–114.
- (44) Ziaie, B.; Baldi, A.; Lei, M.; Gu, Y.; Siegel, R. A. Hard and Soft Micromachining for BioMEMS: Review of Techniques and Examples of Applications in Microfluidics and Drug Delivery. *Adv. Drug Delivery Rev.* **2004**, *56* (2), 145–172.
- (45) Xia, Y.; Whitesides, G. M. Soft Lithography. *Angew. Chem., Int. Ed.* **1998**, *37* (5), 550–575.
- (46) Qin, D.; Xia, Y.; Whitesides, G. M. Soft Lithography for Microand Nanoscale Patterning. *Nat. Protoc.* **2010**, *5* (3), 491–502.
- (47) Zadpoor, A. A. Mechanical Meta-Materials. *Mater. Horiz.* **2016**, 3 (5), 371–381.
- (48) Christensen, J.; Kadic, M.; Kraft, O.; Wegener, M. Vibrant Times for Mechanical Metamaterials. MRS Commun. 2015, 5 (3), 453–462.

- (49) Zheng, X.; Lee, H.; Weisgraber, T. H.; Shusteff, M.; DeOtte, J.; Duoss, E. B.; Kuntz, J. D.; Biener, M. M.; Ge, Q.; Jackson, J. A.; et al. Ultralight, Ultrastiff Mechanical Metamaterials. *Science* **2014**, *344* (6190), 1373–1377.
- (50) Schoen, A. H. *Infinite Periodic Minimal Surfaces Without Self-Intersections*; Technical Note TN D-5541; NASA: Washington, DC, 1970; pp 1–91.
- (51) Cignoni, P.; Callieri, M.; Corsini, M.; Dellepiane, M.; Ganovelli, F.; Ranzuglia, G. MeshLab: An Open-Source Mesh Processing Tool. *Eurographics Ital. Chapter Conf.* **2008**, 129–136.
- (52) Ghosh, M.; Mittal, K. L. Synthesis. In *Polyimides: Fundamentals and Applications*; Marcel Dekker Inc.: New York, 1996; pp 7-187.
- (53) Harris, F. W. Synthesis of Aromatic Polyimides from Dianhydrides and Diamines. In *Polyimides*; Chapman and Hall: New York, 1990; pp 1–37.
- (54) Swyngedau, S.; Nussinovitch, A.; Peleg, M. Models for the Compressibility of Layered Polymeric Sponges. *Polym. Eng. Sci.* **1991**, 31 (2), 140–144.
- (55) Gibson, L. J.; Ashby, M. F. Cellular Solids: Structure and Properties; Cambridge University Press: 1999.
- (56) Fan, H.; Hartshorn, C.; Buchheit, T.; Tallant, D.; Assink, R.; Simpson, R.; Kissel, D. J.; Lacks, D. J.; Torquato, S.; Brinker, C. J. Modulus—Density Scaling Behaviour and Framework Architecture of Nanoporous Self-Assembled Silicas. *Nat. Mater.* **2007**, *6* (6), 418–423
- (57) Qin, Z.; Jung, G. S.; Kang, M. J.; Buehler, M. J. The Mechanics and Design of a Lightweight Three-Dimensional Graphene Assembly. *Sci. Adv.* **2017**, 3 (1), e1601536.